ACS Sustainable Chemistry & Engineering

Research Article

pubs.acs.org/journal/ascecg

Amorphous MnO_2 Modified Biochar Derived from Aerobically Composted Swine Manure for Adsorption of Pb(II) and Cd(II)

Jie Liang,*[,†,‡] Xuemei Li,[†,‡] Zhigang Yu,[§] Guangming Zeng,*[,†,‡] Yuan Luo,[†,‡] Longbo Jiang,[†,‡] Zhaoxue Yang,[†,‡] Yingying Qian,[†,‡] and Haipeng Wu[∥]

[†]College of Environmental Science and Engineering, Hunan University, No. 8 South Lushan Road, Yuelu District, Changsha 410082, P. R. China

[‡]Key Laboratory of Environmental Biology and Pollution Control, Ministry of Education, Hunan University, No. 8 South Lushan Road, Yuelu District, Changsha 410082, P. R. China

[§]Department of Civil and Environmental Engineering, The Hong Kong University of Science and Technology, Clear Water Bay, Sai Kung, Hong Kong, P. R. China

[∥]Changjiang River Scientific Research Institute, No. 23 Huangpu Road, Jiangan District, Wuhan 430010, P. R. China

Supporting Information

ABSTRACT: This study reports creative preparation of MnO_2-biochar (MBR) via MnO_2 modification of biochar (BR) derived from aerobically composted swine manure. SEM coupled with EDX analyzer, TEM, XRD, BET, and FT-IR were employed to examine the surface properties and pore structures of MBR and BR. Adsorption experiments of Pb(II) and Cd(II) including isotherms, kinetics, and thermodynamics as well as the influence of pH on zeta-potential were also investigated. The results indicated that MBR showed rougher and larger surface area and pore volume than BR. In batch adsorption, MBR showed superior adsorption performance (maximum capacity for Pb 268.0 mg/g and Cd 45.8 mg/g) to BR (Pb 127.75 and Cd 14.41 mg/g). The adsorption process was pH-dependent, and the removal efficiency reached its maximum at 0.2 g/L dosage of MBR, after which it declined. Finally, X-ray photoelectron spectrometer (XPS) studies indicated the oxidative Mn^{4+} on MBR, and suggested that apart from electrostatic attachment, specific adsorption (i.e., Pb/Cd−O or hydroxyl binding) and ion exchange were the removal mechanisms of metal ions. Therefore, this modification method toward BR was promising for wastewater treatment of heavy metal pollution.

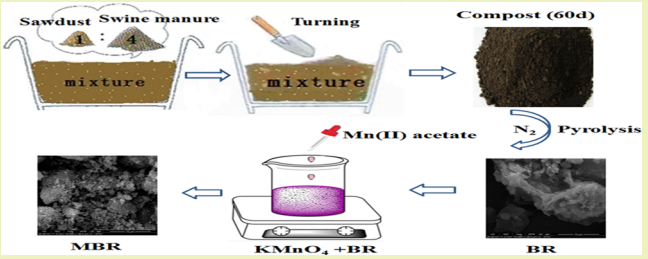

KEYWORDS: *Adsorption, Pb(II), Cd(II), Biochar modification, MnO_2*

INTRODUCTION

With the rapid development of urbanization and industrialization, large amounts of industrial and sewage effluents containing heavy metals are released into surface and underground water. This remains a troubling global environmental problem as a result of their toxicity, nonbiodegradable properties, and even the bioenrichment risk through the food chain.[1−3] Thus, the search for an effective treatment of heavy metals has become of great importance. Of heavy metals produced through anthropogenic activities, lead (Pb) and cadmium (Cd) are considered the most harmful for human health and pervasive contaminants in aqueous environments and soils.[4−6]

Among various water treatment technologies for removing heavy metals, adsorption is a prevailing approach for its simple operation and high efficiency.[1,7,8] During the past decades, researchers have developed various adsorbents exhibiting strong adsorption affinity for heavy metals in aqueous solutions, such as zeolite,[9] iron oxides,[4] activated carbon, and other carbon-based materials.[10−13] However, most of them are limited in practical application because they are time-consuming and very costly. Thus, many efforts have been made to develop novel adsorbents with high adsorption capacity and abundant resources.

Biochar produced via thermochemical pyrolysis of waste biomass with an oxygen-free atmosphere has received increasing attention for its environmentally friendly, cost-effective, and highly efficient superiority. Biomass such as agricultural residues,[14] water hyacinth,[5] sewage sludge, pig manure, and other materials can be converted into biochar through pyrolysis.[15] Nowadays, some researchers have tried to produce biochars from anaerobically digested sugar cane bagasse,[16] algae-dairy-manure,[17] sugar beet tailings,[14] and pig manure.[15] The results showed that biochars derived from anaerobically digested residue have stronger adsorption affinity for contaminants in comparison to the undigested biochars.[14]

Received: February 11, 2017
Revised: April 4, 2017
Published: April 25, 2017

DOI: 10.1021/acssuschemeng.7b00434
ACS Sustainable Chem. Eng. 2017, 5, 5049−5058

Similar to anaerobic digestion, aerobic compost is a process by which organics are broken down into simple inorganic matter with the effect of microbiology, which has easier control and lower cost compared to anaerobic digestion.[18] However, the research on biochar produced from aerobically composted residue is limited.

Although biochar has many attractive advantages such as abundant sources and especially surface groups, fresh carbons cannot cover the high efficiency of pollutant removal since they have inferior surface structures including lower surface area and pore volume. Therefore, studies have concentrated on designing biochar-based composites with improved properties, new structures, and enhanced adsorption capacity by combining biochar with MgO,[19] Fe_3O_4/γ-Fe_2O_3,[4,20,21] AlOOH,[10] carbon materials, and so on.[22] Manganese oxides prevalently exist in terrestrial environments and have better performance than iron oxides with similar surface areas in removal of heavy metals.[23] Meanwhile, the composites based on manganese oxides have been extensively used as effective adsorbents.[24] On the basis of these observations, a composite composed of manganese oxide and biochar would be expected as an adsorbent with high potential. To the best of our knowledge, some researchers had tried direct pyrolysis of pretreated biomass feedstock, which was immersed in the manganese salt solution.[23,24] They synthesized manganese-oxide-modified biochar with large surface area and pore volume, and the as-obtained biochar showed excellent crystallinity and also high ash contents. However, the adsorption capacities of these composites were unattractive since this low removal efficiency probably accounted for the high ash content which was inevitably produced during pyrolysis and limited the removal efficiency of biochar. In addition, this process could be time and energy consuming, could cause the waste of manganese salt solution, and could have difficulty reaching the expected load level.

In this work, we fabricated a MnO_2 modified biochar through a rapid redox reaction between $KMnO_4$ and Mn(II) acetate solution. The load level could be controlled by adjusting the amount of chemical reagent. It can also introduce amorphous MnO_2 without any heat because of the better adsorption performance of amorphous oxides as compared to that of their crystals.[4] A previous study reported that $KMnO_4$ used in the reaction was not only as a reactant but also as a strong oxidizing agent to promote the reactants entering the inner pores of biochar.[1] Thus, it could contribute to the homogeneous dispersion of MnO_2 on pristine biochar. The objectives of the present work are to (1) prepare and characterize two sorbents including biochar derived from aerobically composted swine manure and MnO_2-biochar composite produced by comproportionation process of manganese elements, (2) compare the Pb(II) and Cd(II) removal ability of the composite with that of pristine biochar, and (3) explore the possible adsorption mechanisms through analyzing physico-chemical properties.

MATERIALS AND METHODS

Materials. The pyrolysis feedstock of biochar was obtained from an aerobically composted mixture at the maturing phase (60 days) with the composting ratio of sawdust to swine manure as 1:4 (w/w, fresh weight). This feedstock was bought from a compound organic fertilizer company in Hangzhou, Zhejiang Province, China. The sawdust was used not only as a bulking agent to reduce the water percent of swine manure but also as a low moisture carbon rich material to adjust the ratio of carbon and nitrogen. The design and procedures of the aerobically composting experiment were similar to those of Meng et al.[18] The mixture was dried in an oven at 80 °C for 24 h, and then ground to obtain an average particle size of 0.145 mm and stored before use.

Synthesis of Biochar and MnO_2 Modified Biochar. To get biochar (BR) samples, the composted mixture was pyrolyzed in a tube furnace under flowing N_2 with a heating rate of 10 °C min^{-1} and held at a peak temperature of 400 °C for 2 h. The MnO_2 modified biochar (MBR) was prepared as follows (the loading level was 30 wt %): 15 g of BR and 3.16 g of $KMnO_4$ were mixed in 150 mL of deionized water with vigorous stirring at room temperature, and then the suspension was ultrasonically oscillated for 0.5 h to ensure the full contact of BR and $KMnO_4$; the $KMnO_4$ as a strong oxidizing agent may promote the incorporation.[1] After that, 100 mL of Mn(II) acetate tetrahydrate solution (0.3 M) was added dropwise under continuous stirring, producing dark brown precipitation of MnO_2 in the suspension according to eq 1.[25]

$$3Mn^{2+} + 2MnO_4^- + 2H_2O = 5MnO_2 \downarrow + 4H^+ \quad (1)$$

Finally, the suspension was heated to 80 °C, and was kept at this temperature for an additional 30 min to get the MBR suspension before filtration. In addition, BR and MBR were then washed with deionized (DI) water several times and oven-dried at 80 °C.

Characterizations. The morphologies and sizes of the samples were characterized by field emission scanning electron microscopy (FE-SEM S4800, Hitachi, Japan) equipped with an energy-dispersive X-ray analyzer to fulfill element microanalysis and transmission electron microscopy (TEM, Tecnai G2 F20, FEI). The surface charge of the MBR was determined by measuring the zeta-potential (Zetasizer 300 Hs Malvern, Southborough, MA). The X-ray diffraction (XRD) patterns were collected to identify any crystallographic structures for the samples by using a powder X-ray diffractometer with Cu Kα radiation (XRD, D8 ADVANCE, Bruker). Fourier transform infrared spectroscopy (FT-IR, Nicolet IS10) was used to identify the surface organic functional groups of BR. X-ray photoelectron spectroscopy (XPS) measurements were made with a spectrometer (Thermo Fisher Scientific Kα 1063) equipped with an Al Kα X-ray as the excitation source. The surface areas were detected by N_2 adsorption isotherms at 77 K using an Automated Gas Sorption Anlyzer (Autosorb-IQ, Quantachrome) and calculated by the Brunauer–Emmett–Teller (BET) method. The Barret–Joyner–Halender (BJH) method was used to determine the pore size distribution from the N_2 desorption isotherms. The thermal stability of the samples was tested by thermal gravimetric analysis (TGA) (TG209, Netzsch, Shanghai, China).

Batch Adsorption Experiments and Analysis. Batch adsorption experiments were undertaken to study the effects of heavy metal adsorption by MBR (or BR) samples in 150 mL conical flasks which were sealed and agitated in a temperature-controlled shaker at 170 rpm. The pH-dependent adsorption experiments were conducted with a wider pH range (pH 2–8) adjusted by 0.1 M HNO_3 and NaOH solution. The effect of adsorbent dosage was investigated by varying dosage (10, 20, 50, 100, and 200 mg) at fixed pH (5 ± 0.1) under the temperature of 25 °C. The adsorption kinetics were carried out by controlling the contact time of heavy metal solution and adsorbent at different time intervals (5–2160 min); the mixture contained 20 mg of adsorbent and 50 mL of Pb(II) solution (150 mg/L) or Cd(II) solution (50 mg/L) in 0.01 mol/L $NaNO_3$ as a background electrolyte. For investigation of the adsorption isotherm, the adsorption experiments were performed at (25 ± 1) °C with the equilibrium time of 12 h. The initial concentration of Pb(II) in the solution was in the range 0.5–210 mg/L, while the concentrations of Cd(II) solution ranged from 0.5 to 100 mg/L. The effects of temperature on adsorption of heavy metals were monitored over the temperature range 25–45 °C. After adsorption, the mixtures were filtered through 0.22 μm pore size nylon membrane filters (GE cellulose nylon membrane), and the filtrates were subsequently preserved in 2% HNO_3. Heavy metal concentrations in the filtrates were determined by an atomic absorption spectrophotometer (AAS, z-

DOI: 10.1021/acssuschemeng.7b00434
ACS Sustainable Chem. Eng. 2017, 5, 5049–5058

8100, Hitachi). All results were expressed as the mean value of three replicates. The amounts of heavy metal adsorbed onto the adsorbent and removal efficiency were calculated according to the following equations:

$$q_e = \frac{V(C_0 - C_e)}{W} \quad (2)$$

$$\text{removal efficiency} = \frac{C_0 - C_e}{C_0} \times 100\% \quad (3)$$

where q_e (mg/g) is the amount of heavy metal adsorbed at equilibrium; V (mL) is the volume of solution; C_0 and C_e (mg/L) are the initial and equilibrium heavy metal concentrations in solution; and W (mg) is the mass of adsorbent.

RESULTS AND DISCUSSION

Characterizations of Adsorbents. In order to investigate the morphological structure and surface elemental composition, BR and MBR particles were observed by SEM-EDX. The SEM image (Figure S1a in Supporting Information) shows that BR has a porous structure and smoother surface compared with those of MBR, while the surface of MBR was evenly covered with small particles, which were not found on the BR surface. EDX analysis (Figure S1b,d) shows the changes of elementary composition percentages and confirms the occurrence of elemental Mn on MBR as the EDX spectra showed a strong peak for Mn, where the atomic percentages of Mn and O on the surface obviously increased. The TEM images corresponded with the morphology as presented in the SEM images. The TEM images suggested the mesoporous structure and smooth edge of BR (Figure S2a,b), whereas the surfaces of MBR (Figure S2c,d) were uniformly dispersed with flocculent grains, which could increase the surface area of the composites and provide more contact with contaminants.[11,19]

XRD measurements were performed to investigate the crystal structure of samples. The XRD pattern of BR showed several peaks, which proved the presence of SiO_2, $CaCO_3$, KCl, and MgO (Figure 1a). The results are also consistent with EDX spectra of the BR. It is found that the pattern of BR (Figure 1a) has more and stronger peaks than that of MBR (Figure 1b), and no peaks in MBR refer to the loaded crystalline MnO_2. The weaker peaks in MBR may be caused by the load of the amorphous MnO_2, which could affect the X-ray diffraction of other crystals.[26] The results indicate that the MnO_2 is a nonstoichiometric amorphous phase, similar to the findings of Richter et al.[27] However, MnO_2 loaded in other ways could have several peaks referring to crystalline MnO_2 in the XRD pattern.[1] The difference could be caused by the change of the Mn phase in the preparation of MBR.[25]

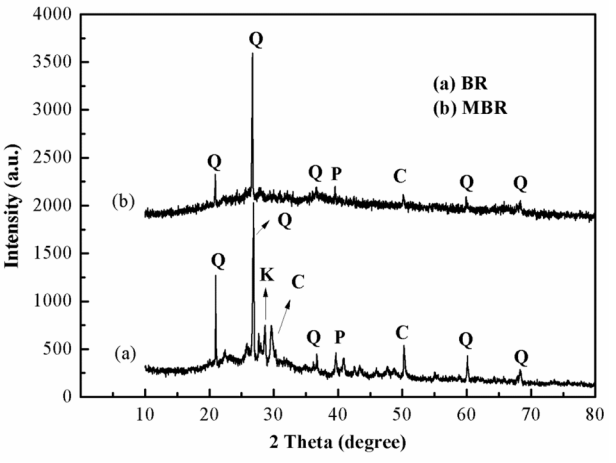

Figure 1. X-ray diffraction of BR (a) and MBR (b). Crystallites were detected with peaks labeled Q for SiO_2, C for $CaCO_3$, K for KCl, and P for MgO.

The properties of BR and MBR can be further discriminated through the surface functional groups as determined by FT-IR spectroscopy. The FT-IR pattern shown in Figure 2 reveals the presence of oxygen-containing functional groups. The broad band around 3368−3429 cm^{-1} corresponds to the OH stretching vibration,[17] while the bands at around 2927 and 1049 cm^{-1} are attributed to the CH_2 deformation vibration and C—O stretching vibrations of polysaccharides, respectively.[14,24] There are C═C and carboxyl C═O stretching vibrations around 1620 and 1386 cm^{-1}.[11,15] In addition, the band around 826 cm^{-1} is due to the C—H aromatic group,[16] and the vibrational property of the Mn—O bond is observed at around 511 cm^{-1}.[28] This result suggests that the surface of BR has been covered by MnO_2.

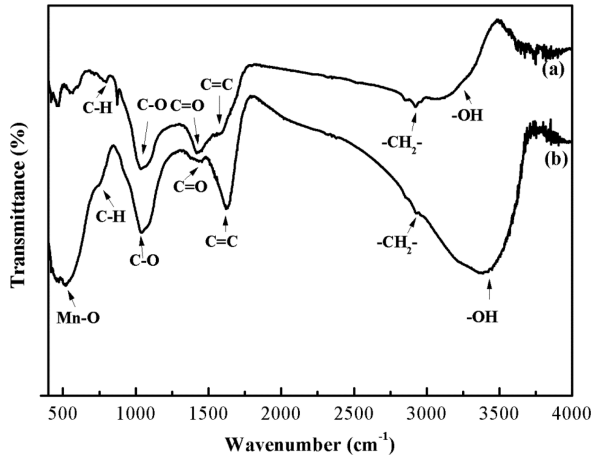

Figure 2. FT-IR spectra of BR (a) and MBR (b).

The BET surface area and corresponding BJH pore size distribution plots of BR and MBR were shown in Figure S3. It was found that the BET surface area and total pore volume of MBR were 70.9096 m^2/g and 0.2398 cm^3/g, which are both about 14 times those of BR (5.0831 m^2/g and 0.0168 cm^3/g). This significant increase of BET surface area could be due to the formation of Mn-bearing minerals,[23] which was proven by the elemental Mn in the EDAX spectrum (Figure S1) and TEM graphs (Figure S2) that indicated the successful coating of MnO_2 on the BR surface (circularly marked in Figure S2c,d). Some researchers found that $KMnO_4$ might cause the destruction of some nanopore structures and transform some nanopores into meso- or macropores because of its strong oxidative property,[17,24] but in this study the average pore diameters of BR and MBR were 13.9536 and 12.8372 nm, respectively, which are different from those findings. This may be attributed to the load of MnO_2 heavily blocking the micropores and reducing the pore diameter of MBR. In addition, the increase of pore volume was helpful for the substance diffusing into the inner pore system of the sorbents, and a larger surface area with more interfaces may be used as potential amendments to adsorb contaminants.

DOI: 10.1021/acssuschemeng.7b00434
ACS Sustainable Chem. Eng. 2017, 5, 5049−5058

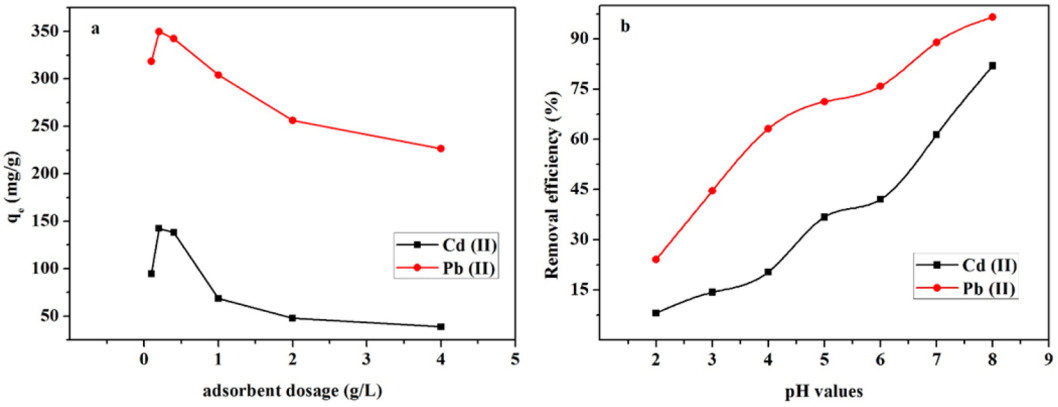

Figure 3. Effect of MBR dosage (a) and pH (b) on the adsorption of Cd(II) and Pb(II).

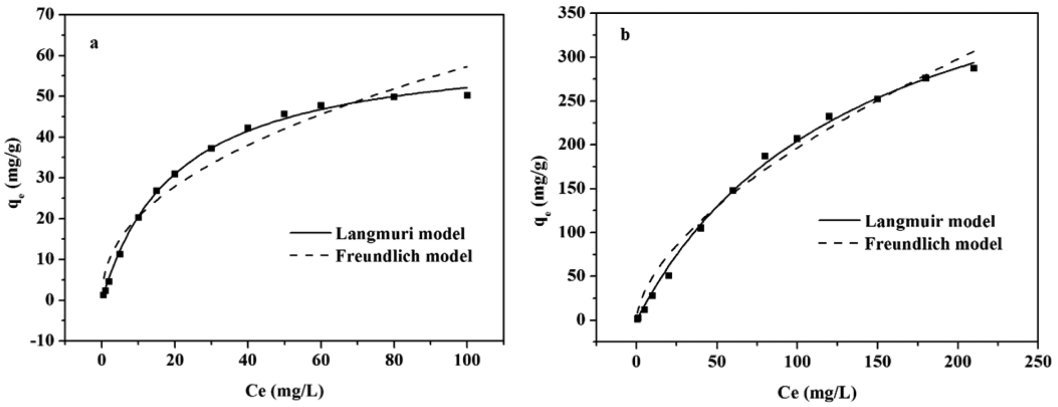

Figure 4. Adsorption isotherms of (a) Cd(II) and (b) Pb(II) onto MBR. Both adsorption conditions were at T = 25 °C, pH = 5 ± 0.2, and ion strength 0.01 M.

The thermogravimetric analysis pattern is shown in Figure S4. It could be seen that the weight percent of BR and MBR decreased with the temperature from 20 to 800 °C. This may be caused by the decomposition of inorganic salts such as ammonium salts and functional groups in BR and MBR. In addition, the weight percent of MBR declined dramatically after 500 °C; this could be attributed to the decomposition of loaded MnO_2 in MBR. To get the content of MnO_2 in the composite, it will be analyzed by XPS later.

Effects of Adsorbent Dose and pH. As depicted in Figure 3a, it was observed that the adsorption capacity of Pb(II) and Cd(II) increased with the dosage of MBR from 0.1 to 0.2 g/L before a marginal decrease at 0.4 g/L. This was because the adsorption sites and pores of the MBR were fully occupied and inaccessible by Pb(II) and Cd(II), though there were enough Pb(II) and Cd(II) ions in aqueous solution. When the MBR dose increased from 0.4 to 4 g/L, the Pb(II) and Cd(II) adsorption capacities decreased drastically and then presented a stable trend. The result may be attributed to the fact that a high MBR dosage promoted the sedimentation and inhibited the diffusion of Pb(II) and Cd(II) to the surface and pore of the MBR. Thus, the appropriate dose of the MBR for the heavy metal removal was found to be 0.2 g/L. However, considering the experimental error and operability, 0.4 g/L was chosen as the dose in the following experiments.

As shown in Figure 3b, the pH effect on the adsorption of Pb(II) and Cd(II) onto the MBRs was performed by adjusting the initial pH of solution to the values of 2, 3, 4, 5, 6, 7, and 8. It was found that the adsorption is a highly pH-dependent process as the removal efficiency increased continuously as the pH values change from 2 to 8. A sharp increase of heavy metal removal efficiency was observed when the pH value increased from 2 to 5. This trend is similar to previous studies in that it was due to the weak effect of adsorption competing with H_3O^+ at low pH 2.[1,29] The hydroxyl groups were gradually deprotonated with changes of pH, which can contribute to the adsorption of heavy metals. Figure 3b also showed that there was no apparent change of metal removal rates between the treatments at pH 5 and 6. This could be caused by the deprotonation of hydroxyl groups reaching the maximum. It indicated that no special acidification for the aqueous solutions is required during the heavy metal removal with MBR. The removal efficiency increased drastically when the pH is above 6, which could be caused by the precipitation of heavy metals during the removal process. Previous studies have shown that lead and cadmium start to precipitate [as $Pb(OH)_2$ and $Cd(OH)_2$] when the solution pH is beyond 6.[30] However, there are several hydrolyzing species with different charges such as $Pb(OH)^+$, $Pb(OH)_2$, $Cd(OH)^+$, $Cd_2(OH)_3^+$, and $Cd(OH)_2$. Thus, heavy metals can be possibly removed by simultaneous precipitation and electrostatic interaction of metal ions and hydrolyzates.[31,32]

The zeta-potential analysis of MBR before and after adsorption was shown in Figure S5. It indicated that the surface of fresh MBR is negatively charged throughout the whole examined pH range, and the pH_{pzc} (point of zero charge) is approximately 1.6, which is conducive to the sorption of cations like Pb(II) and Cd(II). This result is similar to the

DOI: 10.1021/acssuschemeng.7b00434
ACS Sustainable Chem. Eng. 2017, 5, 5049−5058

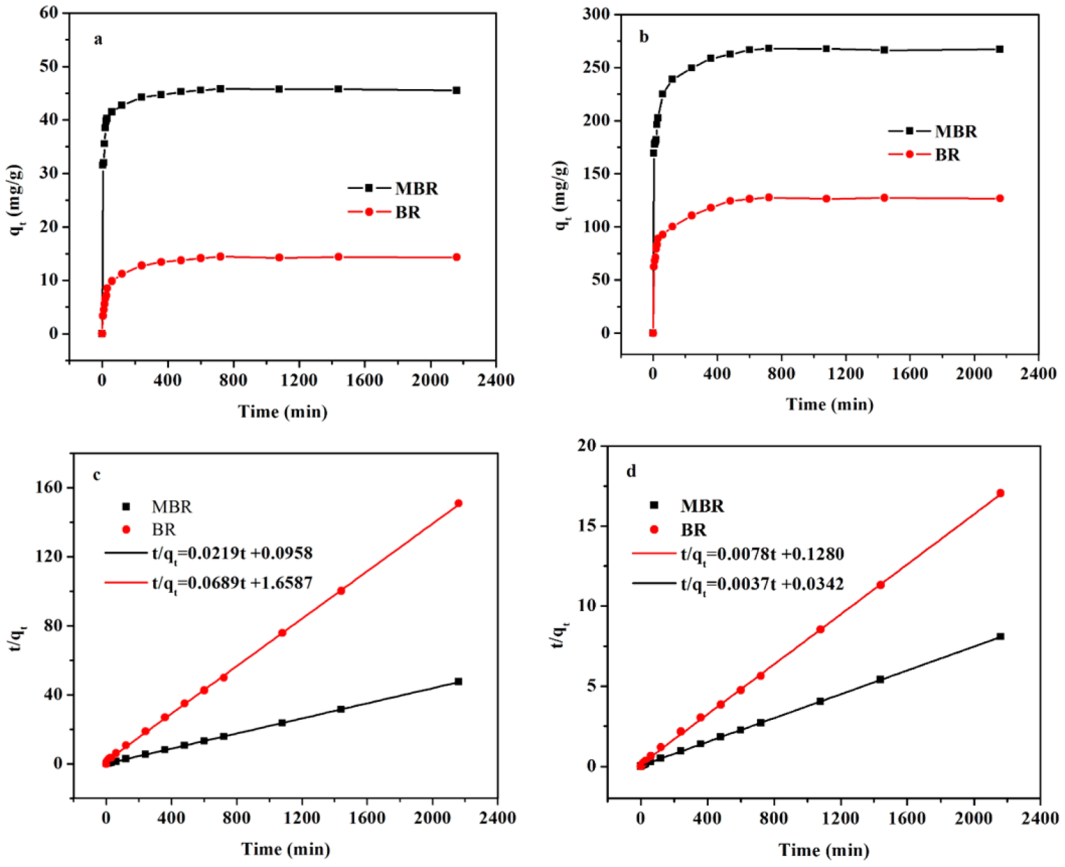

Figure 5. Influence of adsorption time on the removal process of (a, c) Cd(II) and (b, d) Pb(II) by BR and MBR. (c, d) The fitting curves of the pseudo-second-order model.

finding of Yao et al.,[14] and the variation trend of zeta-potential is in good agreement with the pH picture (Figure 3b). The zeta-potential of MBR and MBR-Cd(II) decreased with increasing pH due to the addition of OH^-. As the pH changed from 2 to 4, the zeta-potential of MBR-Pb(II) increased, followed by a stable plateau over pH 4−6, and then it declined with pH between 6 and 7 before increasing again at above 7. The difference of zeta-potentials between MBR-Cd(II) and MBR-Pb(II) was possible due to the different adsorption quantity, which suggested that metal ions were adsorbed as cationic that could neutralize the surface negative charge or formation of metal−ligand composite complexes with metal ions.[33,34] Meanwhile, the electrostatic attraction between the positive metal ion and the oxygen atoms of MnO_2 also did favor the adsorption.[31] Moreover, the surface precipitation and complexation between carboxylic group, hydroxyl, and metal ion also facilitated the adsorption.[35]

Adsorption Isotherms. To give insights into the adsorption of heavy metals onto the synthesized MBR at a constant temperature, the commonly used two-parameter Langmuir and Freundlich models were simulated in the isotherm study. Similar to the previous study, the adsorption edges of Pb(II) and Cd(II) experienced an initial fast ratio and then slow period. Compared to the Freundlich simulation in Figure 4, the experimental data was better followed with the Langmuir model, which could be confirmed by R^2 (0.9974, 0.9977, respectively).

As shown in Figure 4a, Cd(II) sorption increased with the increase of its concentration before the C_e approached 60 mg/L, which indicated the surface saturation toward Cd(II). The results fitted by those two models were displayed in Table S1 (in Supporting Information), which showed that the maximum adsorption amount of Cd(II) onto MBR was 62.83 mg/g. This adsorption capacity on Cd(II) is comparable to that of many other adsorbents listed in Table S2. The hickory biochar modified by $KMnO_4$ (the surface including crystal MnO_2 and Mn_3O_4) had an adsorption capacity of only 28.1 mg/g in spite of having a significant larger surface area (205 m^2/g)[1] than MBR (70.9096 m^2/g). This may be due to the synthesis method and the deposition of synthesized MnO_2 on composted biochar that enhanced the adsorption sites for the attachment of the Cd ion. Figure 4b showed that Pb(II) experienced the same trend, but more rapidly than Cd(II), and the adsorption curve could be fitted well by the two models each with R^2 > 0.99. High adsorption capacity of MBR (Langmuir-based 486.38 mg/g) made it a promising adsorbent to remove Pb(II) from the water medium since it was much higher than that of the previous studies (Table S2). Wang et al. (2015) employed Mn-oxide-modified pine biochar (MPB) and birnessite-modified pine biochar (BPB) to remove Pb(II) with the adsorption maximum of only 4.91 mg/g (MPB) and 47.05 mg/g (BPB), though the surface areas of the two adsorbents were 463.1 and 67.4 m^2/g, respectively.[23] Another research study also reported that the modified BR via coupling of $KMnO_4$ and slow pyrolysis (600 °C) of hickory wood showed the maximum sorption capacity of 34.2 mg/g with the surface area 205 m^2/g.[1] This result also suggested that the obtained MnO_2 provided more active adsorption sites for Pb(II) and Cd(II), and the specific surface area of adsorbent determined little adsorption performance toward contaminants.

DOI: 10.1021/acssuschemeng.7b00434
ACS Sustainable Chem. Eng. 2017, 5, 5049−5058

Table 1. Kinetic Parameters of Pb(II) and Cd(II) Adsorption on MBR and BR Based on the Pseudo-Second-Order Model and Intraparticle Diffusion Model

		pseudo-second-order kinetics			intraparticle diffusion model					
adsorbent	M(II)	$q_{e,exp}$ (mg/g)	$q_{e,cal}$ (mg/g)	R^2	$k_{i,1}$	R^2	$k_{i,2}$	R^2	$k_{i,3}$	R^2
BR	Cd	14.41	14.51	0.9998	0.4964	0.9928	0.1563	0.9856	0.0061	0.9158
	Pb	127.75	128.21	0.9999	0.1878	0.9882	0.1395	0.9945	0.0070	0.9773
MBR	Cd	45.8	45.66	0.9999	0.1404	0.9971	0.0354	0.9665	0.0061	0.9868
	Pb	268.0	270.27	0.9997	0.0987	0.9857	0.0598	0.9535	0.0027	0.9771

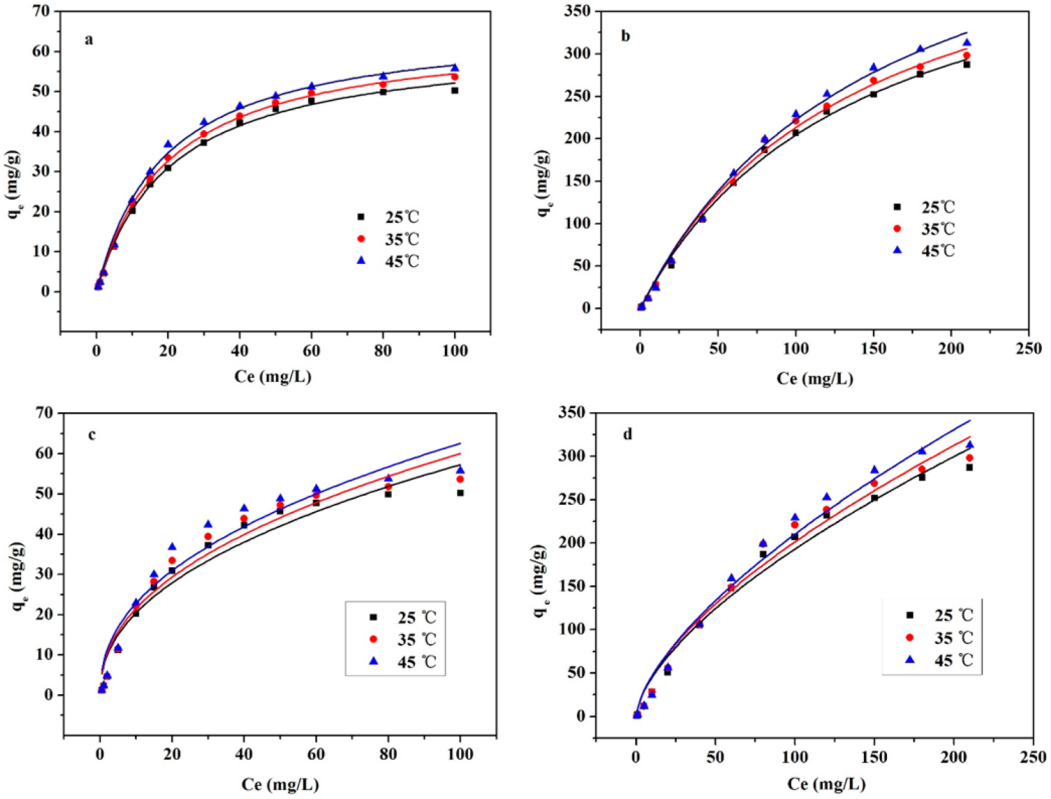

Figure 6. Thermodynamics of Pb(II) and Cd(II) sorption isotherms onto MBR: (a, c) Cd(II) and (b, d) Pb(II). Equilibrium conditions: MBR concentration 0.4 g/L, pH = 5.0, and ion strength 0.01 M. Pb(II) and Cd(II) initial concentrations ranged from 0.5 to 210 and 100 mg/L, respectively. Langmuir and Freundlich curve models were employed to fit the experiment results.

Adsorption Kinetics. To understand the adsorption process of Pb(II) and Cd(II) onto MBR, the sorption kinetics was employed as a function of elapsed time (Figure 5). Similar to the results of a previous study, Figure 5a,b showed that the adsorption of Pb(II) and Cd(II) exhibited an initial rapid period, followed by a relatively short decreasing step before reaching stability at 400 min. The adsorption capacities of MBR on Pb and Cd were notable in a short period of 60 min (230 and 41.5 mg/g, respectively), which was larger than that for the previous adsorbents.[23,36,37] The fast step was caused by the solution diffusion of adsorbates and exterior surface adsorption on adsorbents, whereas the second one could be interpreted by the resistance of heavy metal ions that diffused to the interior of porous adsorbents.[4] Obviously, the adsorption performance of MBR toward two heavy metals was superior to that of unmodified BR (Figure 5a,b), and especially, the adsorption efficiencies of Pb(II) and Cd(II) by the MBR were twice and four times that of BR, respectively. This was consistent with the result of the isothermal experiment and indicated a great enhancement effect by MnO_2.

A pseudo-second-order model has been intensively used to simulate and analyze the adsorption process. This model can be depicted as follows.[10]

$$\frac{t}{q_t} = \frac{1}{(k_2 q_e^{\,2})} + \frac{1}{q_e} t \tag{4}$$

Here, the following abbreviations apply: q_t and q_e are the adsorption amount at time t and at equilibrium, respectively; k_2 represents the rate constant. Herein, this fit well with the data (Figure 5c,d) with R^2 no less than 0.99 after modification of the model equation, and the kinetic parameters were shown in Table 1. The calculated adsorption capacity [$q_{e,cal}$ (mg/g)] was perfectly close to the experimental counterparts [$q_{e,exp}$ (mg/g)].

Moreover, a three-step intraparticle diffusion model was also used to give insights into the mechanism and rate-limiting phases during the adsorption process. It can be seen from Figure S6 that the curve edges were all divided into three linear periods with their own rate constants, which were listed in Table 1. It showed that the adsorption rates followed the order $k_{i,1} > k_{i,2} > k_{i,3}$ for Pb(II) and Cd(II) adsorption onto BR and

DOI: 10.1021/acssuschemeng.7b00434
ACS Sustainable Chem. Eng. 2017, 5, 5049−5058

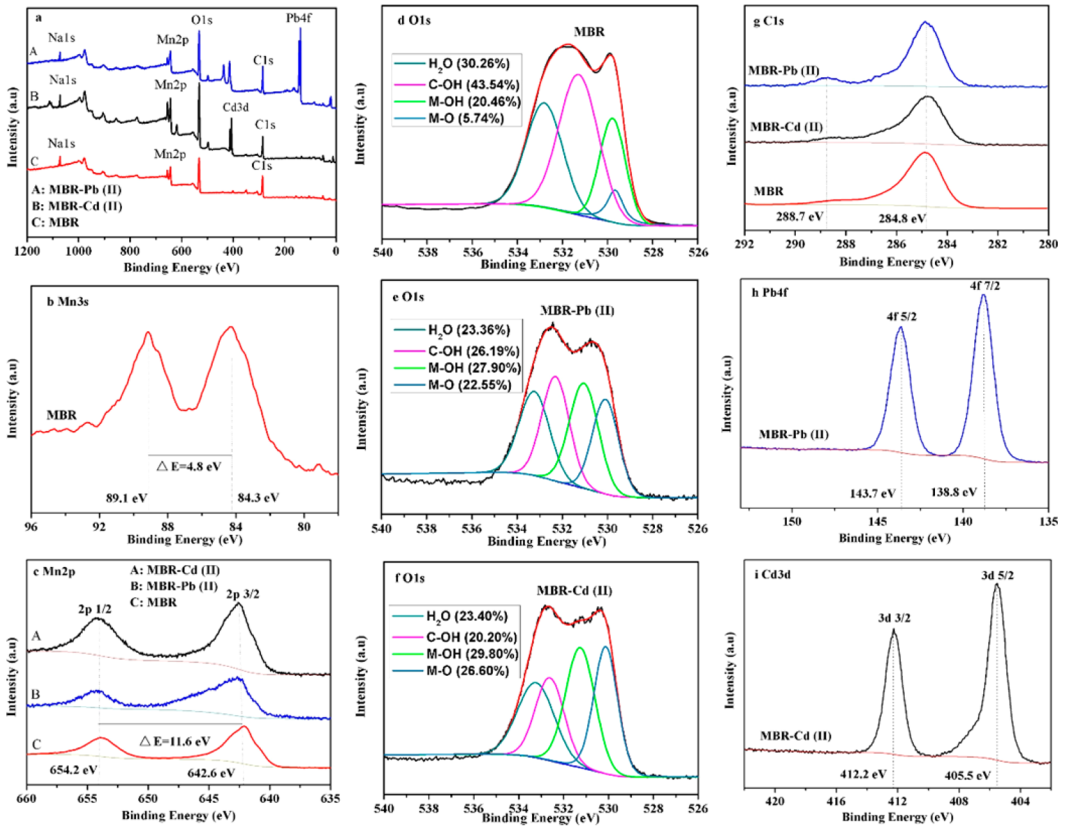

Figure 7. XPS scan of MBR before and after adsorption for Pb(II), Cd(II): (a) wide scan, (b) Mn 3s, (c) Mn 2p, (d) O 1s for MBR, (e) O 1s for MBR-Pb(II), (f) O 1s for MBR-Cd(II), (g) C 1s, (h) Pb 4f, and (i) Cd 3d.

MBR, which was consistent with previous studies.[4,10] Similar to the result from pseudo-second-order analysis, the initial fast stage indicated the exterior surface adsorption of adsorbates diffusing from solution. This was followed by a second one, or a decline of diffusion rates ($k_{i,2}$), during which the removal amount of metal ions had approached the maximum. As the adsorbates were adsorbed on the exterior surface, fewer active sites were available for the coming adsorbates, and simultaneously, the adsorbed metal ions could further enter into the mesoporous interior of MBR and BR, leading to more diffusion resistance. Finally, the adsorption equilibrium capacity was reached, and adsorption rates stayed at the least $k_{i,3}$. This is also because the content of Pb(II) and Cd(II) decreased in solution. In addition, Table 1 showed that Cd(II) was removed faster than Pb(II), although the removal efficiency was the opposite. This was also evident in Figure 5a,b. MBR showed a higher adsorption rate than BR because MBR had more active adsorption sites for Pb(II) and Cd(II), and higher specific area and pore volume may contribute to the contact of MBR with ions; then, there is less resistance for ions to diffuse onto the surface of MBR. These results suggested that the modification of MnO_2 toward BR is efficient and necessary.

Adsorption Thermodynamics. Reaction temperature plays a significant role in reaction rate and adsorption efficiency. In this study, different temperatures (25, 35, and 45 °C) were chosen to study the adsorption phenomenon. Two equilibrium models were also used to quantitatively analyze the adsorption process. As shown in Figure 6, adsorption capacities at all the temperatures showed marginal differences, but the removal amounts of MBR for Pb(II) and Cd(II) increased with the increasing reaction temperatures from 25 to 45 °C. This was different from a previous study showing that the removal capacity of biochar derived from sewage sludge pyrolysis at 900 °C showed no remarkable differences under various temperatures.[38] This enhanced adsorption performance with increasing temperature indicated the endothermic adsorption process can promote the diffusion of ions in solution and also the availability of the active surface sites at high temperature.[4] Additionally, the Langmuir model with a higher correlation coefficient (R^2) fitted better to the thermodynamic isotherm data than the Freundlich model (shown in Table S3). The calculated q_m (mg/g) of the Langmuir model exhibited a slight uptrend with an increase of temperature, and the capacity at 25 °C was close to that of the equilibrium isotherm analyzed above. This result suggested the stable adsorption behavior of MBR.

According to the modified van't Hoff isothermal equation,[39] thermodynamic parameters such as Gibbs free energy (ΔG), enthalpy (ΔH), and entropy (ΔS) were calculated. The calculated results were listed in Table S4, and positive ΔG and ΔS could be found, indicating a nonspontaneous process and the increase of randomness at the interface between solid and solution. Interestingly, ΔH was negative for Pb(II) but turned positive for Cd(II), which was contrary to the endothermic adsorption mentioned above. This may suggest that high temperature did strengthen the binding of Pb(II) on adsorbents. High values of ΔG and ΔH suggested chemisorption for Pb(II) and Cd(II) removal.

XPS Analysis. To give insights into the metallic state of element Mn in MBR and the mechanism of adsorption, XPS analysis was employed for the MBR before and after adsorption. Figure 7a showed the full-range scale spectrum of

DOI: 10.1021/acssuschemeng.7b00434
ACS Sustainable Chem. Eng. 2017, 5, 5049−5058

MBR and MBR with loading Pb(II) and Cd(II). It could be seen that element Na existed in both BR and MBR, but its content was higher in the former than in the latter (results in EDX). Since Na has a strong ion exchange ability to replace cations such Pb(II) and Cd(II),[40] the ionic exchange process of BR was more obvious than that of MBR. As shown in Figure 7b, the two peaks observed in the range 78−96 eV were assigned as the Mn 3s state. The separation 4.8 eV indicated that the Mn oxide species in MBR was MnO_2.[41] Expanded spectra of element Mn 2p were shown in Figure 7c, which displayed double peaks at the binding energy values of 642.6 and 654.2 eV. The separation between Mn $2p_{3/2}$ and Mn $2p_{1/2}$ of 11.6 eV indicated that the predominant Mn oxidation state in synthesized MBR was Mn^{4+},[42,43] which was consistent with Mn 3s. This was different from a previous study that showed an immersion-heat modification of $KMnO_4$ on BR with a single peak at 642.0 eV,[24] but was similar to an engineered BR from $KMnO_4$ treated biomass.[1] In addition, the content of MnO_2 (MBR, 38%; MBR-Cd(II), 32%) could be calculated by Mn atomic percent of MBR (7.39%), MBR-Pb(II) (7.84%), and MBR-Cd(II) (7.51%), respectively. This was quite close to the expected value that is from stoichiometric calculation of eq 1. The O 1s spectrum (Figure 7d−f) was divided into four peaks located at 530.1, 531.4, 532.4, and 533.2 eV, which can be assigned to metal oxide (M—O), hydroxyl bonded to metal (M—OH), hydroxyl on MBR surface (C—OH), and adsorbed H_2O in the adsorbent, respectively.[24,44] It was found that the area ratio of C—OH decreased from 43.54% to 26.19% or 20.20% after Pb(II) or Cd(II) adsorption, respectively. However, the area ratio of M—OH and M—O increased after Pb(II) (M—OH, 20.46−27.90%; M—O, 5.74%−22.55%) or Cd(II) (M—OH, 20.46−29.80%; M—O, 5.74%−26.60%) adsorption. To the best of our knowledge, metal adsorption on the adsorbent should increase the area ratio of M—OH with the assumption of no hydroxyl groups on the metal oxide disappeared during the adsorption process, and the increase of M—O could be attributed to the formation of Mn—O—R (R: functional groups), Pb—O, or Cd—O groups on the MBR surface after adsorption. The decrease of oxygen in C—OH suggested that hydroxyl groups that existed in BR surely participated in the adsorption. The ratios of H_2O in MBR-Pb(II) and MBR-Cd(II) were similar since the adsorbed H_2O is not involved in the adsorption, but were different from MBR for the change of other forms of oxygen. The locations of two peaks of the C 1s scan (Figure 7g) were at 284.8 and 288.7 eV, corresponding to the graphite C and O═C—O,[45,46] respectively, which would provide abundant active adsorption sites.

In addition, seldom has research examined the species of adsorbed heavy metals on the surface of adsorbents. Here, Pb(II) and Cd(II) adsorption by MBR was analyzed. XPS of Pb 4f and Cd 3d in Figure 7h,i showed the same result as a former report, which suggested specific sorption, especially in the form of Pb/Cd−O or hydroxyl binding, also explained the mechanism of Pb(II) and Cd(II) removal by obtained adsorbents.[4]

CONCLUSIONS

A novel approach to synthesize amorphous MnO_2 modified biochar was conducted. The obtained MBR showed rough surface, larger surface area, and pore volume, and better adsorption performance than BR. This adsorption process was highly pH-dependent and was better fit by the Langmuir model than by the Freundlich model in both isotherms and thermodynamics. Specific adsorption in the form of Pb/Cd−O or hydroxyl binding and ion exchange were the adsorption mechanism of Pb(II) and Cd(II). Results from the present research indicated that MnO_2 modification can be potentially used to remove heavy metals from polluted water.

ASSOCIATED CONTENT

Supporting Information

The Supporting Information is available free of charge on the ACS Publications website at DOI: 10.1021/acssuschemeng.7b00434.

Characterization of adsorbents including SEM-EDX, TEM, BET, and TGA patterns; three-step intraparticle diffusion model and zeta-potential pictures; adsorption parameters; and comparison of different adsorbents (PDF)

AUTHOR INFORMATION

Corresponding Authors

*E-mail: liangjie82@163.com. Phone: +86 731 88821413. Fax: +86 731 88823701.

*E-mail: zgming@hnu.edu.cn. Phone: +86 731 88823701. Fax: +86 731 88823701.

ORCID

Jie Liang: 0000-0003-4559-4378

Notes

The authors declare no competing financial interest.

ACKNOWLEDGMENTS

The researchers was thankful for being supported by the National Natural Science Foundation of China (51479072, 51679082, 51521006, 51579094, and 51579098). We also appreciated the valuable comments and suggestions from other anonymous reviewers to enhance the quality of this paper.

REFERENCES

(1) Wang, H.; Gao, B.; Wang, S.; Fang, J.; Xue, Y.; Yang, K. Removal of Pb(II), Cu(II), and Cd(II) from aqueous solutions by biochar derived from $KMnO_4$ treated hickory wood. *Bioresour. Technol.* **2015**, *197*, 356−362.

(2) Zhang, C.; Yu, Z. G.; Zeng, G. M.; Jiang, M.; Yang, Z. Z.; Cui, F.; Zhu, M. Y.; Shen, L. Q.; Hu, L. Effects of sediment geochemical properties on heavy metal bioavailability. *Environ. Int.* **2014**, *73*, 270−281.

(3) Hua, S.; Liang, J.; Zeng, G.; Xu, M.; Zhang, C.; Yuan, Y.; Li, X.; Li, P.; Liu, J.; Huang, L. How to manage future groundwater resource of China under climate change and urbanization: An optimal stage investment design from modern portfolio theory. *Water Res.* **2015**, *85*, 31−37.

(4) Zhang, C.; Yu, Z. G.; Zeng, G. M.; Huang, B. B.; Dong, H. R.; Huang, J. H.; Yang, Z. Z.; Wei, J. J.; Hu, L.; Zhang, Q. Phase transformation of crystalline iron oxides and their adsorption abilities for Pb and Cd. *Chem. Eng. J.* **2016**, *284*, 247−259.

(5) Zhang, F.; Wang, X.; Yin, D.; Peng, B.; Tan, C.; Liu, Y.; Tan, X.; Wu, S. Efficiency and mechanisms of Cd removal from aqueous solution by biochar derived from water hyacinth (Eichornia crassipes). *J. Environ. Manage.* **2015**, *153*, 68−73.

(6) Liang, J.; Zhong, M.; Zeng, G.; Chen, G.; Hua, S.; Li, X.; Yuan, Y.; Wu, H.; Gao, X. Risk management for optimal land use planning integrating ecosystem services values: A case study in Changsha, Middle China. *Sci. Total Environ.* **2017**, *579*, 1675−1682.

(7) Tang, W. W.; Zeng, G. M.; Gong, J. L.; Liang, J.; Xu, P.; Zhang, C.; Huang, B. B. Impact of humic/fulvic acid on the removal of heavy

metals from aqueous solutions using nanomaterials: a review. *Sci. Total Environ.* **2014**, *468−469*, 1014−1027.
(8) Yu, Z.; Zhang, C.; Zheng, Z.; Hu, L.; Li, X.; Yang, Z.; Ma, C.; Zeng, G. Enhancing phosphate adsorption capacity of SDS-based magnetite by surface modification of citric acid. *Appl. Surf. Sci.* **2017**, *403*, 413−425.
(9) Alver, E.; Metin, A. Ü. Anionic dye removal from aqueous solutions using modified zeolite: Adsorption kinetics and isotherm studies. *Chem. Eng. J.* **2012**, *200−202*, 59−67.
(10) Liang, J.; Liu, J.; Yuan, X.; Dong, H.; Zeng, G.; Wu, H.; Wang, H.; Liu, J.; Hua, S.; Zhang, S.; et al. Facile synthesis of alumina-decorated multi-walled carbon nanotubes for simultaneous adsorption of cadmium ion and trichloroethylene. *Chem. Eng. J.* **2015**, *273*, 101−110.
(11) Tang, J.; Lv, H.; Gong, Y.; Huang, Y. Preparation and characterization of a novel graphene/biochar composite for aqueous phenanthrene and mercury removal. *Bioresour. Technol.* **2015**, *196*, 355−363.
(12) Tang, W. W.; Zeng, G. M.; Gong, J. L.; Liu, Y.; Wang, X. Y.; Liu, Y. Y.; Liu, Z. F.; Chen, L.; Zhang, X. R.; Tu, D. Z. Simultaneous adsorption of atrazine and Cu (II) from wastewater by magnetic multi-walled carbon nanotube. *Chem. Eng. J.* **2012**, *211−212*, 470−478.
(13) Wang, H.; Yuan, X.; Wu, Y.; Zeng, G.; Chen, X.; Leng, L.; Li, H. Synthesis and applications of novel graphitic carbon nitride/metal-organic frameworks mesoporous photocatalyst for dyes removal. *Appl. Catal., B* **2015**, *174−175*, 445−454.
(14) Yao, Y.; Gao, B.; Inyang, M.; Zimmerman, A. R.; Cao, X.; Pullammanappallil, P.; Yang, L. Biochar derived from anaerobically digested sugar beet tailings: characterization and phosphate removal potential. *Bioresour. Technol.* **2011**, *102*, 6273−6278.
(15) Xu, X.; Cao, X.; Zhao, L.; Sun, T. Comparison of sewage sludge- and pig manure-derived biochars for hydrogen sulfide removal. *Chemosphere* **2014**, *111*, 296−303.
(16) Inyang, M.; Gao, B.; Pullammanappallil, P.; Ding, W.; Zimmerman, A. R. Biochar from anaerobically digested sugarcane bagasse. *Bioresour. Technol.* **2010**, *101*, 8868−8872.
(17) Jin, H. M.; Hanif, M. U.; Capareda, S.; Chang, Z. Z.; Huang, H. Y.; Ai, Y. C. Copper(II) removal potential from aqueous solution by pyrolysis biochar derived from anaerobically digested algae-dairy-manure and effect of KOH activation. J. Environ. *J. Environ. Chem. Eng.* **2016**, *4*, 365−372.
(18) Meng, J.; Wang, L.; Liu, X.; Wu, J.; Brookes, P. C.; Xu, J. Physicochemical properties of biochar produced from aerobically composted swine manure and its potential use as an environmental amendment. *Bioresour. Technol.* **2013**, *142*, 641−646.
(19) Zhang, M.; Gao, B.; Yao, Y.; Xue, Y.; Inyang, M. Synthesis of porous MgO-biochar nanocomposites for removal of phosphate and nitrate from aqueous solutions. *Chem. Eng. J.* **2012**, *210*, 26−32.
(20) Yang, J.; Zhao, Y.; Ma, S.; Zhu, B.; Zhang, J.; Zheng, C. Mercury Removal by Magnetic Biochar Derived from Simultaneous Activation and Magnetization of Sawdust. *Environ. Sci. Technol.* **2016**, *50*, 12040−12047.
(21) Liu, W. J.; Tian, K.; Jiang, H.; Yu, H. Q. Facile synthesis of highly efficient and recyclable magnetic solid acid from biomass waste. *Sci. Rep.* **2013**, *3*, 2419.
(22) Yuan, X.; Wang, H.; Wu, Y.; Chen, X.; Zeng, G.; Leng, L.; Zhang, C. A novel SnS_2−$MgFe_2O_4$/reduced graphene oxide flower-like photocatalyst: Solvothermal synthesis, characterization and improved visible-light photocatalytic activity. *Catal. Commun.* **2015**, *61*, 62−66.
(23) Wang, S.; Gao, B.; Li, Y.; Mosa, A.; Zimmerman, A. R.; Ma, L. Q.; Harris, W. G.; Migliaccio, K. W. Manganese oxide-modified biochars: preparation, characterization, and sorption of arsenate and lead. *Bioresour. Technol.* **2015**, *181*, 13−17.
(24) Song, Z.; Lian, F.; Yu, Z.; Zhu, L.; Xing, B.; Qiu, W. Synthesis and characterization of a novel MnO_x-loaded biochar and its adsorption properties for Cu^{2+} in aqueous solution. *Chem. Eng. J.* **2014**, *242*, 36−42.
(25) Wang, S.; Gong, W.; Liu, X.; Yao, Y.; Gao, B.; Yue, Q. Removal of lead(II) from aqueous solution by adsorption onto manganese oxide-coated carbon nanotubes. *Sep. Purif. Technol.* **2007**, *58*, 17−23.
(26) Escande, V.; Petit, E.; Garoux, L.; Boulanger, C.; Grison, C. Switchable Alkene Epoxidation/Oxidative Cleavage with H_2O_2/$NaHCO_3$: Efficient Heterogeneous Catalysis Derived from Biosourced Eco-Mn. ACS Sustain. *ACS Sustainable Chem. Eng.* **2015**, *3*, 2704−2715.
(27) Richter, M.; Berndt, H.; Eckelt, R.; Schneider, M.; Fricke, R. Zeolite-mediated removal of NO_x by NH_3 from exhaust streams at low temperatures. *Catal. Today* **1999**, *54*, 531−545.
(28) Wei Hsu, B. Y.; Wang, M.; Zhang, Y.; Vijayaragavan, V.; Wong, S. Y.; Yuang-Chi Chang, A.; Bhakoo, K. K.; Li, X.; Wang, J. Silica-F127 nanohybrid-encapsulated manganese oxide nanoparticles for optimized T_1 magnetic resonance relaxivity. *Nanoscale* **2014**, *6*, 293−299.
(29) Inyang, M.; Gao, B.; Yao, Y.; Xue, Y.; Zimmerman, A. R.; Pullammanappallil, P.; Cao, X. Removal of heavy metals from aqueous solution by biochars derived from anaerobically digested biomass. *Bioresour. Technol.* **2012**, *110*, 50−56.
(30) Tiwari, D.; Laldanwngliana, C.; Choi, C.-H.; Lee, S. M. Manganese-modified natural sand in the remediation of aquatic environment contaminated with heavy metal toxic ions. *Chem. Eng. J.* **2011**, *171*, 958−966.
(31) Gupta, V. K.; Agarwal, S.; Saleh, T. A. Synthesis and characterization of alumina-coated carbon nanotubes and their application for lead removal. *J. Hazard. Mater.* **2011**, *185*, 17−23.
(32) Su, Y.; Adeleye, A. S.; Huang, Y.; Sun, X.; et al. Simultaneous removal of cadmium and nitrate in aqueous media by nanoscale zerovalent iron (nZVI) and Au doped nZVI particles. *Water Res.* **2014**, *63*, 102−111.
(33) Wang, Z.; Lee, S. W.; Catalano, J. G.; Lezama-Pacheco, J. S.; Bargar, J. R.; Tebo, B. M.; Giammar, D. E. Adsorption of uranium(VI) to manganese oxides: X-ray absorption spectroscopy and surface complexation modeling. *Environ. Sci. Technol.* **2013**, *47*, 850−858.
(34) Chen, G. C.; Shan, X. Q.; Wang, Y. S.; Wen, B.; Pei, Z. G.; Xie, Y. N.; Liu, T.; Pignatello, J. J. Adsorption of 2,4,6-trichlorophenol by multi-walled carbon nanotubes as affected by Cu(II). *Water Res.* **2009**, *43*, 2409−2418.
(35) Gao, Z.; Bandosz, T. J.; Zhao, Z.; Han, M.; Qiu, J. Investigation of factors affecting adsorption of transition metals on oxidized carbon nanotubes. *J. Hazard. Mater.* **2009**, *167*, 357−365.
(36) Wang, P.; Tang, L.; Wei, X.; Zeng, G.; Zhou, Y.; Deng, Y.; Wang, J.; Xie, Z.; Fang, W. Synthesis and application of iron and zinc doped biochar for removal of p-nitrophenol in wastewater and assessment of the influence of co-existed Pb(II). *Appl. Surf. Sci.* **2017**, *392*, 391−401.
(37) Clemente, J. S.; Beauchemin, S.; MacKinnon, T.; Martin, J.; Johnston, C. T.; Joern, B. Initial biochar properties related to the removal of As, Se, Pb, Cd, Cu, Ni, and Zn from an acidic suspension. *Chemosphere* **2017**, *170*, 216−224.
(38) Chen, T.; Zhou, Z.; Han, R.; Meng, R.; Wang, H.; Lu, W. Adsorption of cadmium by biochar derived from municipal sewage sludge: Impact factors and adsorption mechanism. *Chemosphere* **2015**, *134*, 286−293.
(39) Fan, L.; Luo, C.; Sun, M.; Qiu, H.; Li, X. Synthesis of magnetic beta-cyclodextrin-chitosan/graphene oxide as nanoadsorbent and its application in dye adsorption and removal. *Colloids Surf., B* **2013**, *103*, 601−607.
(40) Wang, T.; Liu, W.; Xiong, L.; Xu, N.; Ni, J. Influence of pH, ionic strength and humic acid on competitive adsorption of Pb(II), Cd(II) and Cr(III) onto titanate nanotubes. *Chem. Eng. J.* **2013**, *215−216*, 366−374.
(41) Biesinger, M. C.; Payne, B. P.; Grosvenor, A. P.; Lau, L. W. M.; Gerson, A. R.; Smart, R. S. C. Resolving surface chemical states in XPS analysis of first row transition metals, oxides and hydroxides: Cr, Mn, Fe, Co and Ni. *Appl. Surf. Sci.* **2011**, *257*, 2717−2730.
(42) Zhou, L.; Huang, Y.; Qiu, W.; Sun, Z.; Liu, Z.; Song, Z. Adsorption Properties of Nano-MnO_2-Biochar Composites for Copper in Aqueous Solution. *Molecules* **2017**, *22*, 173.

DOI: 10.1021/acssuschemeng.7b00434
ACS Sustainable Chem. Eng. 2017, 5, 5049−5058

(43) Han, R.; Zou, W.; Zhang, Z.; Shi, J.; Yang, J. Removal of copper(II) and lead(II) from aqueous solution by manganese oxide coated sand I. Characterization and kinetic study. *J. Hazard. Mater.* **2006**, *137*, 384−395.
(44) Ren, Y.; Yan, N.; Feng, J.; Ma, J.; Wen, Q.; Li, N.; Dong, Q. Adsorption mechanism of copper and lead ions onto graphene nanosheet/δ-MnO_2. *Mater. Chem. Phys.* **2012**, *136*, 538−544.
(45) Xia, Y.; Meng, L.; Jiang, Y.; Zhang, Y.; Dai, X.; Zhao, M. Facile preparation of MnO_2 functionalized baker's yeast composites and their adsorption mechanism for Cadmium. *Chem. Eng. J.* **2015**, *259*, 927−935.
(46) Wang, J.; Tang, L.; Zeng, G.; Liu, Y.; Zhou, Y.; Deng, Y.; Wang, J.; Peng, B. Plasmonic Bi Metal Deposition and g-C_3N_4 Coating on Bi_2WO_6 Microspheres for Efficient Visible-Light Photocatalysis. ACS Sustain. *Chem. Eng.* **2017**, *5*, 1062−1072.

DOI: 10.1021/acssuschemeng.7b00434
ACS Sustainable Chem. Eng. 2017, 5, 5049−5058